



Title	Aerodynamic instability of an inflatable aeroshell in suborbital re-entry
Author(s)	Takahashi, Yusuke; Ohashi, Tatsushi; Oshima, Nobuyuki; Nagata, Yasunori; Yamada, Kazuhiko
Citation	Physics of fluids, 32(7), 075114 https://doi.org/10.1063/5.0009607
Issue Date	2020-07-01
Doc URL	http://hdl.handle.net/2115/82107
Rights	This article may be downloaded for personal use only. Any other use requires prior permission of the author and AIP Publishing. This article appeared in Physics of Fluids 32, 075114 (2020) and may be found at https://aip.scitation.org/doi/10.1063/5.0009607 .
Type	article
File Information	5.0009607.pdf



[Instructions for use](#)

Aerodynamic instability of an inflatable aeroshell in suborbital re-entry

Cite as: Phys. Fluids **32**, 075114 (2020); <https://doi.org/10.1063/5.0009607>

Submitted: 01 April 2020 . Accepted: 01 July 2020 . Published Online: 16 July 2020

Yusuke Takahashi , Tatsushi Ohashi, Nobuyuki Oshima, Yasunori Nagata, and Kazuhiko Yamada



[View Online](#)



[Export Citation](#)



[CrossMark](#)

ARTICLES YOU MAY BE INTERESTED IN

[Acoustic-wave-induced cooling in onset of hypersonic turbulence](#)

[Physics of Fluids](#) **32**, 061702 (2020); <https://doi.org/10.1063/5.0011871>

[Experimental investigation of turbulent wake flows in a helically wrapped rod bundle in presence of localized blockages](#)

[Physics of Fluids](#) **32**, 075113 (2020); <https://doi.org/10.1063/5.0008589>

[Recurrence analysis and time extrapolation of a confined turbulent jet using modal decomposition](#)

[Physics of Fluids](#) **32**, 075115 (2020); <https://doi.org/10.1063/5.0010315>



Aerodynamic instability of an inflatable aeroshell in suborbital re-entry

Cite as: Phys. Fluids 32, 075114 (2020); doi: 10.1063/5.0009607

Submitted: 1 April 2020 • Accepted: 1 July 2020 •

Published Online: 16 July 2020



View Online



Export Citation



CrossMark

Yusuke Takahashi,^{1,a)} Tatsushi Ohashi,¹ Nobuyuki Oshima,¹ Yasunori Nagata,² and Kazuhiko Yamada³

AFFILIATIONS

¹ Hokkaido University, Kita 13 Nishi 8, Kita-ku, Sapporo, Hokkaido 060-8628, Japan

² Okayama University, 1-1-1 Tsushima-naka Kita-ku, Okayama, Okayama 700-8530, Japan

³ Japan Aerospace Exploration Agency, 3-1-1 Yoshinodai Chuo-ku, Sagamihara, Kanagawa 252-5210, Japan

^{a)} Author to whom correspondence should be addressed: ytakahashi@eng.hokudai.ac.jp

ABSTRACT

Aerodynamic instability in the attitude of an inflatable re-entry vehicle in the subsonic regime has been observed during suborbital re-entry. This causes significant problems for aerodynamic decelerators using an inflatable aeroshell; thus, mitigating this problem is necessary. In this study, we revealed the instability mechanism using a computational science approach. To reproduce the in-flight oscillation motion in an unsteady turbulent flow field, we adopted a large-eddy simulation approach with a forced-oscillation technique. Computations were performed for two representative cases at transonic and subsonic speeds that were in stable and unstable states, respectively. Pitching moment hysteresis at a cycle in the motion was confirmed for the subsonic case, whereas such hysteresis did not appear for the transonic case. Pressures on the front surface and in the wake of the vehicle were obtained by employing a probe technique in the computations. Pressure phase delays at the surface and in the wake were confirmed as the pitch angle of the vehicle increased (pitch up) and decreased (pitch down), respectively. In particular, we observed that the wake structure formed by a large recirculation behavior significantly affected the pressure phase delay at the rear of the vehicle. The dynamic instability at subsonic speed resulted from flows that could not promptly follow the vehicle motion. Finally, the damping coefficients were evaluated for the design and development of the inflatable vehicle.

Published under license by AIP Publishing. <https://doi.org/10.1063/5.0009607>

NOMENCLATURE

C	aerodynamic coefficient or model constant	\mathbf{Q}	conservative variable vector
d	distance from wall (m)	R	gas constant [J/(kg K)]
D	drag (N) or diameter (m)	S	area (m^2)
E	internal energy (J/m^3)	S_{ij}	strain-rate tensor (1/s)
f	frequency (Hz)	t	time (s)
\mathbf{F}	flux vector	T	temperature (K)
I	moment of inertia (kg m^2)	u, U	velocity (m/s)
k	reduced frequency	V	volume (m^3)
l	length (m)	\mathbf{W}	source term vector
L	lift (N)	x	coordinate (m)
M	pitching moment (N m)	y^+	non-dimensional distance
p	pressure (Pa)	α	angle (rad)
q	heat flux (W/m^2) or dynamic pressure (Pa)	δ_{ij}	Kronecker delta
		Δ	grid scale
		ε_{ijk}	Eddington epsilon

κ	von Karman constant
λ	thermal conductivity [W/(K m)]
μ	viscosity (N s/m ²)
ρ	density (kg/m ³)
τ_{ij}	viscous stress tensor (N/m ²)
ω	angular velocity (rad/s)

Subscripts

D	drag
g	grid move
L	lift
M	pitching
p	pressure
SGS	subgrid scale
v	viscous
∞	freestream

I. INTRODUCTION

An inflatable aeroshell is one of the innovative technologies proposed for atmospheric re-entry missions. An inflatable vehicle can generally achieve a low-ballistic-coefficient flight because of its low mass and large front-projected area. This is due to it having a flexible and lightweight membrane aeroshell. This can provide several advantages, e.g., a decrease in aerodynamic heating^{1,2} and the mitigation of communication blackout³ during the re-entry phase. In addition, critical operations such as parachutes and float extraction are not required in the descent and splashdown phases. To date, several studies on inflatable aeroshell technologies have been conducted. Significant progress includes the tension cone supersonic inflatable aerodynamic decelerator (SIAD),⁴ the attached inflatable decelerator⁴ with an isotensoid structure, the hypersonic inflatable aerodynamic decelerator (HIAD)⁵ with a stacked tori structure, and the inflatable re-entry and descent technology.⁶

A re-entry demonstration using an S-310-41 sounding rocket (SMAAC: Sounding rocket experiment of membrane aeroshell for atmospheric-entry capsule) was conducted.⁷⁻⁹ This mission was a demonstration of a low-ballistic-coefficient flight during re-entry. SMAAC primarily consists of three components: a capsule, a membrane aeroshell, and an inflatable torus (Fig. 1). The capsule has a semispherical configuration with a diameter of 190 mm. The membrane aeroshell has a flare angle of 70° and a frontal projected diameter of 926 mm and is connected to the inflatable torus. The inflatable torus has a tube diameter of 100 mm. After the vehicle is inflated, its overall diameter is 1200 mm.

An attitude instability in the SMAAC mission was observed at subsonic speed.⁸ Figure 2 shows the history of the angle of attack (AOA) of SMAAC. The figure also includes the profiles of Mach number and altitude measured during the mission. First, SMAAC was launched with a sounding rocket. It was separated with an angular velocity of 1.2 Hz around the body axis (i.e., the roll direction) at an altitude of 111 km. SMAAC began to re-enter the atmosphere along a suborbital re-entry trajectory at an altitude of 150 km. It had a high AoA after separation from the rocket. However, in the supersonic regime during re-entry, its AOA tended to decrease. After an

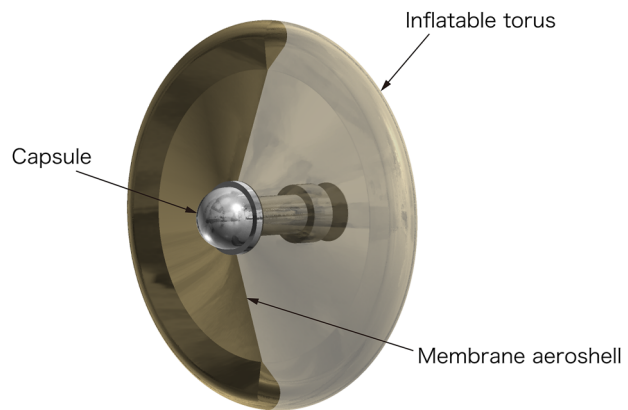


FIG. 1. SMAAC configuration.

elapsed time of 600 s after launch, the AOA rapidly increased. At altitudes between 9.4 km and 3.7 km, which corresponded to elapsed times of 865 s and 1120 s, respectively, SMAAC's attitude behavior became unstable and vertical rotation occurred. Finally, SMAAC's attitude recovered, and the vehicle splashed down in the ocean with a low AOA.

Despite SMAAC being statically stable at all speeds, as reported by Ohashi *et al.*,¹⁰ its attitude was unstable during the mission. This can be attributed to a dynamic instability mode in the attitude. When the oscillation motion of a re-entry vehicle is not damped, dynamic instability can ensue, leading to the divergence of motion. Kazemba *et al.*¹¹ reviewed studies related to dynamic instability, which can be affected by many factors, e.g., the center of gravity (CG), front shape, rear shape, freestream Mach number, and reduced frequency

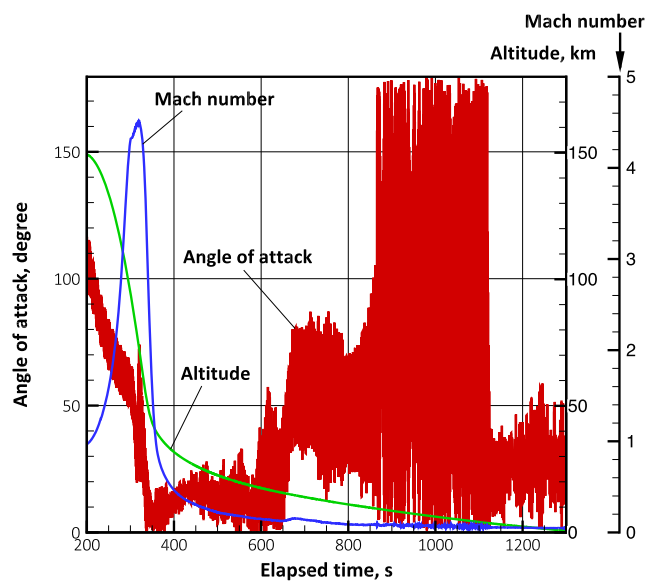


FIG. 2. SMAAC AOA along the suborbital re-entry trajectory.

(Strouhal number). Hiraki¹² investigated the dynamic instability of a Hayabusa-type re-entry capsule in the transonic regime using a transonic wind tunnel. Teramoto *et al.*^{13,14} numerically studied the instability of the Hayabusa capsule using a computational fluid dynamics (CFD) approach. In the simulations, a Reynolds-averaged Navier-Stokes equation (RANS) with a forced oscillation was adopted. In these studies, the effects of the rear shape of the capsule were surveyed. Tsurumoto *et al.*¹⁵ investigated dynamic instability using the large-eddy simulation (LES) and forced-oscillation approaches. Koga *et al.*¹⁶ conducted experiments on the instability of the HTV return vehicle using a transonic wind tunnel. In the experiment, free rotation with a single degree of freedom (DOF) was permitted, and dynamic instability was observed at subsonic speeds. Moreover, Hashimoto *et al.*¹⁷ performed CFD with forced oscillations and then examined the instability mechanism in comparison with the experimental results. Brock *et al.*¹⁸ numerically reproduced a ballistic range experiment for an inflatable aerodynamic decelerator. In their paper, they reported that pressure on the front and rear surfaces caused instability at supersonic speeds. Modal analysis approaches are becoming powerful tools to investigate unsteady turbulent flow fields.^{19,20} Ohmichi *et al.*²¹ revealed the aerodynamic wake structure of a re-entry capsule using the modal analysis approach.

In the future development and design of aerodynamic decelerator vehicles, clarifying and mitigating the dynamic instability mode is critical. However, for inflatable aeroshells, a detailed investigation has not yet been conducted, and the instability mechanism is unclear. The use of the LES technique is effective in reproducing unsteady turbulence around the vehicle during re-entry although the computational cost is significantly high. However, with the recent development in high-performance computers, superior computational resources are becoming available. Moreover, a numerical simulation model to reproduce the complicated turbulent behavior around the inflatable re-entry vehicle has been constructed.^{22,23} In this study, we numerically investigate the instability observed in the SMAAC mission using LES of CFD and forced-oscillation approaches to reveal its mechanism.

II. NUMERICAL METHOD

A. Modeling

The following assumptions were made for the proposed analysis model: (1) The flow is turbulent; (2) the gas considered corresponds to air, which is composed of 0.765 N₂ and 0.235 O₂ in terms of mass fraction; and (3) no chemical reaction occurs.

In this study, we adopted the compressible Navier-Stokes equations and the equation of state to describe the flow fields. The flow field equations were composed of conservation laws of total mass, momentum, and total energy; these can be expressed in integral forms as follows:

$$\frac{d}{dt} \int_V \mathbf{Q} dV + \int_S (\mathbf{F}_j - \mathbf{F}_{vj}) n_j dS = 0, \quad (1)$$

where n_j is the element of the normal vector of area dS . The vectors of the conservative variable \mathbf{Q} , advection flux \mathbf{F} , and viscous flux \mathbf{F}_v

are described as follows:

$$\mathbf{Q} = \begin{bmatrix} \rho \\ \rho u_i \\ E \end{bmatrix}, \quad \mathbf{F}_j = \begin{bmatrix} \rho u_j \\ \rho u_i u_j + \delta_{ij} p \\ (E + p) u_j \end{bmatrix}, \quad \mathbf{F}_{vj} = \begin{bmatrix} 0 \\ \tau_{ij} \\ q_j + u_i \tau_{ij} \end{bmatrix}, \quad (2)$$

where δ_{ij} is the Kronecker delta. In addition, τ_{ij} and q_j in the above equations are the stress tensor and heat flux, respectively, which are expressed as follows:

$$\tau_{ij} = \mu \left(\frac{\partial u_i}{\partial x_j} + \frac{\partial u_j}{\partial x_i} - \frac{2}{3} \frac{\partial u_k}{\partial x_k} \delta_{ij} \right), \quad (3)$$

$$q_j = \lambda \frac{\partial T}{\partial x_j}. \quad (4)$$

The equation of state is expressed as

$$p = \rho R T. \quad (5)$$

The total energy included translational, rotational, vibrational internal, and kinetic energies. The molecular viscosity was evaluated using Sutherland's law. The thermal conductivity was calculated using the viscosity, specific heat at constant pressure, and Prandtl number, which was set to 0.71.

LES was adopted to describe unsteady turbulent flow. The governing equations were filtered using Favre filtering.²⁴ Note that the formulation of Eq. (1) applying the Favre filtering operator is described in detail in Ref. 25. The standard Smagorinsky model²⁶ was used as the subgrid-scale model. In this study, the turbulent eddy viscosity μ_{SGS} was obtained by

$$\mu_{SGS} = \rho L_{SGS}^2 \sqrt{2 \bar{S}_{ij} \bar{S}_{ij}}, \quad (6)$$

where \bar{S}_{ij} is the strain-rate tensor expressed using the mean velocity component, \bar{u}_i . Additionally, L_{SGS} was determined by the mixing length and grid scale Δ , which can be expressed as

$$L_{SGS} = \min(\kappa d, C_s \Delta), \quad (7)$$

where κ , C_s , and d are the von Karman constant ($\kappa = 0.41$), Smagorinsky constant ($C_s = 0.2$), and the distance from the surface, respectively. According to Shur's study,²⁷ the grid scale was given by

$$\Delta = \min[\max(C_w d, C_w \Delta_{\max}, \Delta_{\min}), \Delta_{\max}], \quad (8)$$

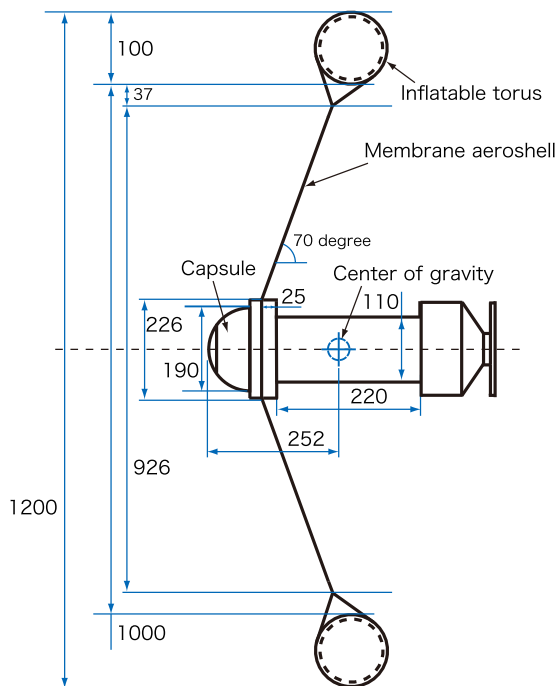
where $C_w = 0.15$, Δ_{\max} is the maximum grid size in the three directions of the x -, y -, and z -axis, and Δ_{\min} is the minimum value. The subgrid-scale thermal conductivity was evaluated by the turbulent eddy viscosity, specific heat at constant pressure, and turbulent Prandtl number of 0.90.

B. Numerical implementation

The software package RG-FaSTAR v2.1.6²⁸ was adopted. It includes a high-enthalpy flow solver that incorporates real gas effects and thermochemical nonequilibrium flow. This software is a version of the fast unstructured CFD code "FaSTAR,"²⁹ originally developed by the Japan Aerospace Exploration Agency (JAXA).

TABLE I. Freestream conditions.

Mach number	Reynolds number	Altitude (km)	Velocity (m/s)	Density (kg/m^3)	Temperature (K)
0.90	1.02×10^5	39.3	286.1	4.76×10^{-3}	250.9
0.13	6.39×10^5	16.1	37.25	1.93×10^{-1}	204.0

**FIG. 3.** Drawing of the SMAAC computational model. (All length dimensions are in millimeters.)

The governing equations of the flow field were solved using a finite-volume approach. All the flow properties were set at the center of a control volume. Spatial gradients of the flow properties were calculated based on the weighted Green–Gauss theorem.

Advection fluxes in the governing equations were calculated using the simple low-dissipation AUSM (SLAU) scheme³⁰ with the monotonic upstream-centered scheme for conservation laws (MUSCL) interpolation method for high accuracy. Viscous fluxes were evaluated using the averaged gradients of the flow variables between two computational cells. Time integration was performed using an implicit time-marching method. A dual-time-stepping method with a second-order backward difference was adopted for time integration in the unsteady state. The lower–upper symmetric Gauss–Seidel (LU-SGS) method was employed as a matrix solver.

To express the motion of the vehicle in the flow field, we modified the governing equations in the noninertial frame by considering the grid movement. The grid velocity of the computational grids in motion was expressed as

$$u_{gj} = \frac{\partial x_j}{\partial t}. \quad (9)$$

Equation (1) can then be modified as follows:

$$\int_V \frac{\partial \mathbf{Q}}{\partial t} dV + \int_S (\mathbf{F}_{gj} - \mathbf{F}_{vj}) n_j dS - \int_S (u_{gj} \mathbf{Q}) n_j dS = \int_V \mathbf{W}_c dV, \quad (10)$$

where \mathbf{W}_c is the source term vector obtained by the Coriolis force,³¹ which is given by

$$\mathbf{W}_c = \begin{bmatrix} 0 \\ -\varepsilon_{ijk} \omega_j \rho u_k \\ 0 \end{bmatrix}, \quad (11)$$

where ε_{ijk} and ω_j are the Eddington epsilon and angular velocity, respectively. The third term on the left-hand side of Eq. (10) was included to satisfy the geometric conservation law.³² In addition, \mathbf{F}_{gj} is the modified advection flux that considers the grid movement. The flow velocity in the advection flux \mathbf{F}_j was modified in \mathbf{F}_{gj} as follows: $u_j \rightarrow u_j - u_{gj}$.

The membrane aeroshell was deformed by the aerodynamic force during flight. However, for the simplicity of the analysis model, no deformation was considered; the membrane was assumed rigid.

C. Computational conditions

The attitude instability of SMAAC was observed in the low-Mach-number region of ~ 0.1 from the trajectory shown in Fig. 2. The calculations above were performed for two representative cases of Mach numbers 0.90 and 0.13, which were stable and unstable, respectively (Table I). In this paper, these cases are referred to as

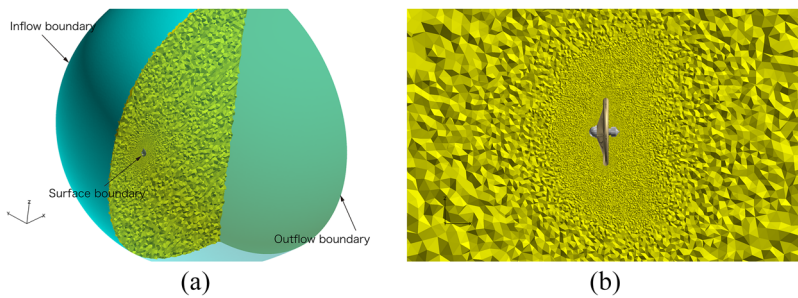
**FIG. 4.** Computational domain and boundaries (a), and grids (b) for SMAAC flow-field simulation.

TABLE II. Forced-oscillation conditions.

Mach number	Frequency (Hz)	Mean angle (deg)	Amplitude (deg)	Reduced frequency
0.90	0.635	10.57	4.89	0.0167
0.13	0.600	27.23	11.76	0.1214

M0.90 and M0.13, respectively. The Reynolds number is defined by $Re = \rho_\infty U_\infty l / \mu_\infty$, where ρ_∞ , U_∞ , μ_∞ , and l are the freestream density, freestream velocity, freestream viscosity, and characteristic length, i.e., SMAAC diameter ($l = 1.2$ m), respectively.

Figure 3 shows a drawing of a SMAAC computational model. The rotation center corresponds to the CG of SMAAC, located at a distance of 252 mm from the capsule head along the body axis.

Figure 4 shows the computational domain depicting the boundary conditions and computational grids for the simulations in this study. The boundaries were composed of inflow, outflow, and surface boundaries. At the inflow, the freestream conditions listed in Table I were applied. A gradient-free condition for all the flow parameters was imposed at the outflow. A nonslip condition for the velocity and a condition of zero-pressure gradient normal to the surface were imposed at the surface. In practice, a boundary condition on the surface considering an acceleration of a body by oscillation is more appropriate.³³ However, because the acceleration of motion was expected to be low in this case, we adopted the zero-gradient condition. The temperature was fixed as 273 K at the surface. The computational grids in the computational domain were composed of a tetrahedral mesh. The numbers of cells for the computational grids for the M0.90 and M0.13 were 17 121 706 and 37 493 715, respectively.

To reproduce the oscillation motion of SMAAC during reentry, we adopted a forced-oscillation method. A single-DOF rotation around the y axis was considered. The AOA was given by

$$\alpha = \alpha_0 + \alpha_1 \sin(2\pi ft), \quad (12)$$

where α , α_0 , α_1 , f , and t are the pitching angle (AOA), mean angle, amplitude, frequency, and time, respectively. These parameters, which are listed in Table II, were obtained by reconstructing the measured AOA profile in the flight using the fast Fourier transform (FFT) for each case. The reduced frequency was defined by

$$k = \frac{2\pi f}{U_\infty}. \quad (13)$$

The freestream velocity at the inflow boundary was modified as follows: $u = U_\infty \cos \alpha$, $v = 0$, and $w = U_\infty \sin \alpha$.

III. RESULTS AND DISCUSSION

In this study, the aerodynamic coefficients were defined by

$$C_D = \frac{D}{\frac{1}{2} \rho_\infty U_\infty^2 S}, \quad (14)$$

$$C_L = \frac{L}{\frac{1}{2} \rho_\infty U_\infty^2 S}, \quad (15)$$

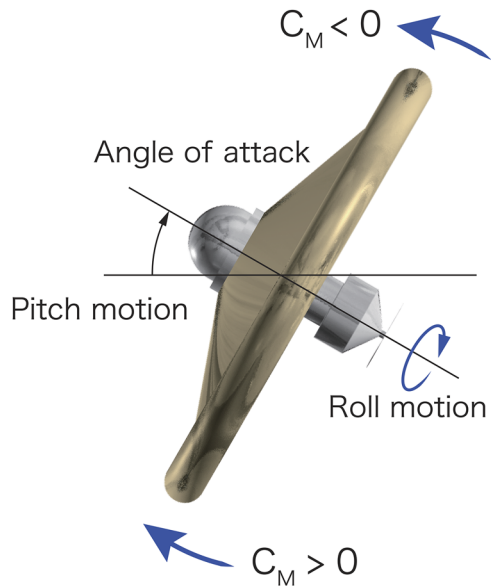


FIG. 5. Definition of the direction of pitching moment with respect to AOA.

$$C_M = \frac{M}{\frac{1}{2} \rho_\infty U_\infty^2 S l}, \quad (16)$$

$$C_p = \frac{P - P_\infty}{\frac{1}{2} \rho_\infty U_\infty^2}, \quad (17)$$

where D , L , and M are the drag force, lift force, and pitching moment, respectively. In addition, p_∞ and S are the freestream pressure and the front-projected area of SMAAC, $\pi(l/2)^2$, respectively. Figure 5 shows the definition of the direction in the pitching moment with respect to the AOA. Additionally, the figure depicts the roll motion around the body axis although the roll was not considered in this simulation.

A. Grid dependency

To investigate the dependency on the computational grids, we conducted a grid study for the Mach numbers of 0.90 and 0.13. The AOAs were set to 20° and 30° for the M0.90 and M0.13 cases, respectively. The numbers of computational grids used in the study are listed in Table III.

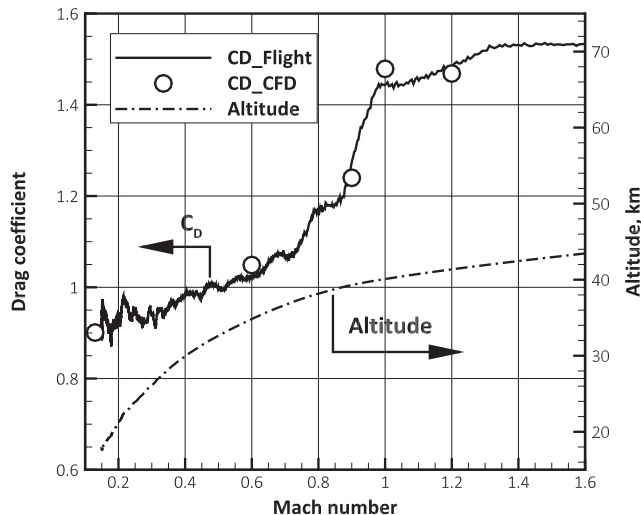
Table IV shows the comparisons of the pitching moment coefficients for M0.90 and M0.13 with each computational grid.

TABLE III. Number of computational grid cells used in this grid study.

Case	Fine grids	Normal grids	Coarse grids
M0.90	56 662 868	17 121 706	11 898 475
M0.13	57 224 176	37 493 715	17 121 706

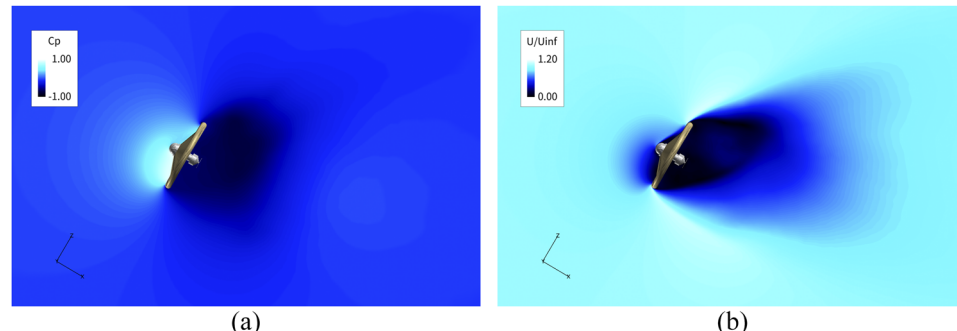
TABLE IV. Comparison of pitching moment coefficients in this grid study.

Case	Fine grids	Normal grids	Coarse grids
M0.90	-3.08×10^{-2}	-3.24×10^{-2}	-3.47×10^{-2}
M0.13	-4.48×10^{-2}	-4.50×10^{-2}	-4.93×10^{-2}

**FIG. 6.** Comparison of drag coefficients between flight data and computed results.**TABLE V.** Comparison of aerodynamic coefficients among the SS, WALE, and no SGS models.

SGS model	C_D	C_L	C_M
SS	8.62×10^{-1}	-4.14×10^{-1}	-4.93×10^{-2}
WALE	4.48×10^{-1}	-3.88×10^{-1}	-1.25×10^{-1}
No model	4.08×10^{-1}	-3.63×10^{-1}	-1.23×10^{-1}

Compared with the results for the fine grid cases, the errors in pitching moment coefficients with normal grids were within $\sim 5\%$. This result indicated that the computational grids used here were sufficiently convergent.

**FIG. 7.** Distribution of time-averaged pressure and velocity around SMAAC for the case of a freestream Mach number of 0.13. (a) Pressure coefficient. (b) Velocity magnitude normalized by freestream velocity.

B. Comparison with flight data

The computed drag coefficients were compared with the measured data in the SMAAC flight to validate the proposed analysis model. Note that the AOA in the computations was fixed at zero. Figure 6 shows the comparison of the drag coefficients between the measured and computed results. In addition to the two cases listed in Table I, computations for three cases of Mach numbers 1.2, 1.0, and 0.6 were also performed. Figure 6 also includes the altitude profile of SMAAC. The drag coefficient tended to have a constant value in the supersonic region but began to decrease rapidly in the transonic region. In the subsonic region, the drag coefficient decreased with the decrease in the Mach number. Excellent agreements between the measured and computed results were confirmed. Reproducing a wake structure for accurate prediction at those speeds is important for inflatable aeroshells.

C. Performance of SGS model

To investigate the contributions of the SGS model to aerodynamic coefficient prediction, flow field simulations with the standard Smagorinsky (SS), wall-adapting local eddy viscosity (WALE),³⁴ and no SGS models were performed at an AOA of 30° for M0.13. The coarse computational grid system was used based on the computational cost. Table V presents the comparison among the drag, lift, and pitching coefficients. The computed results of the WALE and no SGS models were significantly different from those obtained using the SS model. Considering the comparative analysis of the flight experimental results shown in Fig. 6, the present analysis model with SS can properly reproduce aerodynamics.

D. Flow topology

To describe the fundamental structure of the flow field around SMAAC, as the representative case, Figs. 7(a) and 7(b) show the distributions of the pressure coefficient and velocity magnitude normalized by freestream velocity, respectively, for M0.13. These were time-averaged distributions over one period of the third cycle of motion. Because the flows were stagnated, a high-pressure region appeared in front of SMAAC. The flows were separated on the inflatable torus, and then, shear layers were formed behind SMAAC. A large recirculation region was formed in the wake where the pressure largely decreased. For inflatable re-entry vehicles such as

SMAAC, the pressure component of aerodynamic forces including the moments is remarkably larger than the friction component. This is primarily because the surface pressure difference between the front and the rear is increased by the front stagnation and large recirculation regions as mentioned above.

The non-dimensional distances, y^+ , over surfaces of the membrane and inflatable torus were less than 5 and 10, respectively. These are not small when performing LES, in general. However, the turbulent boundary on the membrane was expected to have only a minor role in forming a wake structure. From the perspective of the computational cost, the proposed computational grids were adopted here.

E. Dynamic instability

Because the pitching moment generally contributes significantly to dynamic instability, evaluating this parameter is important. Figures 8(a) and 8(b) show the time histories of the pitching moment coefficient and AOA of SMAAC for M0.90 and M0.13, respectively, in the computations of this study. The figures depict the pitching moment at the third, fourth, and fifth cycles of the motion. Because the results of the first and second cycles possibly included the initial state, they are not discussed here.

The pitching moment for M0.90 promptly followed the change in the AOA. However, Fig. 8 confirms that the pitching moment for M0.13 had a phase delay of $\sim\pi/12$ with respect to change in the AOA. Such a phase delay can induce instability.

Figures 9(a) and 9(b) show the plots of the pitching moment coefficient against the AOA for M0.90 and M0.13, respectively.

These curves were averaged over the three cycles between the third and fifth cycle. In Fig. 9, the red and blue lines indicate the pitching moments with an increase and decrease in AOA, respectively. When the pitching moment with an AOA decrease is lower than that with an AOA increase, the attitude state is unstable, and vice versa.³⁵ In other words, in the figure, a clockwise cycle means a dynamically unstable state, whereas a counterclockwise cycle means a stable state. For M0.90, several crossings of the curve during the cycles were observed. Therefore, damping of the oscillation motion could occur for the case. However, for M0.13, the cycle was always clockwise, and the attitude state was unstable. This meant that the energy of motion was supplied by the flow field, which led to dynamic instability.

To evaluate the energy obtained by SMAAC from the flow field during each cycle of the motion, we calculated the normalized work produced by the pitching moment acting on the AOA, which is given by

$$\bar{W} = \int_C C_M d\alpha. \quad (18)$$

When \bar{W} is negative, because the energy of the motion decreases, damping occurs, which leads to a stable state. However, when \bar{W} is positive, damping does not occur, which leads to a dynamically unstable state. Table VI lists the integral values, \bar{W} , for M0.90 and M0.13. For M0.90, the integral values were always negative, and the motions were stable. In contrast, because \bar{W} for M0.13 was positive, the state was unstable. These results show that the computations reproduced the tendencies of the flight data observed in the SMAAC experiment.

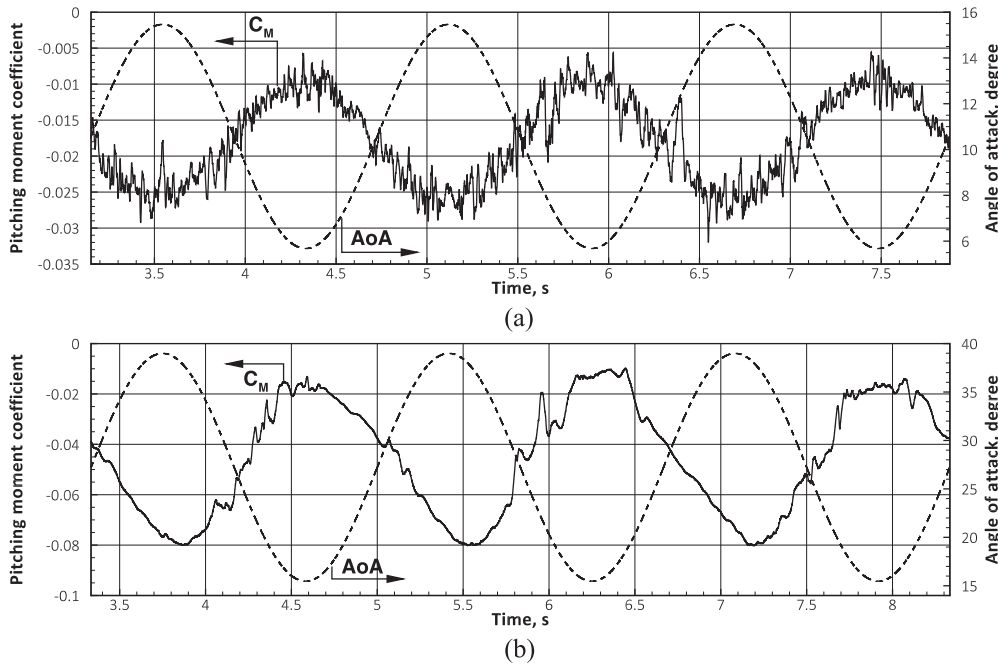


FIG. 8. Histories of pitching moment and AOA of SMAAC for cases of freestream Mach numbers of 0.90 and 0.13. (a) M0.90. (b) M0.13.

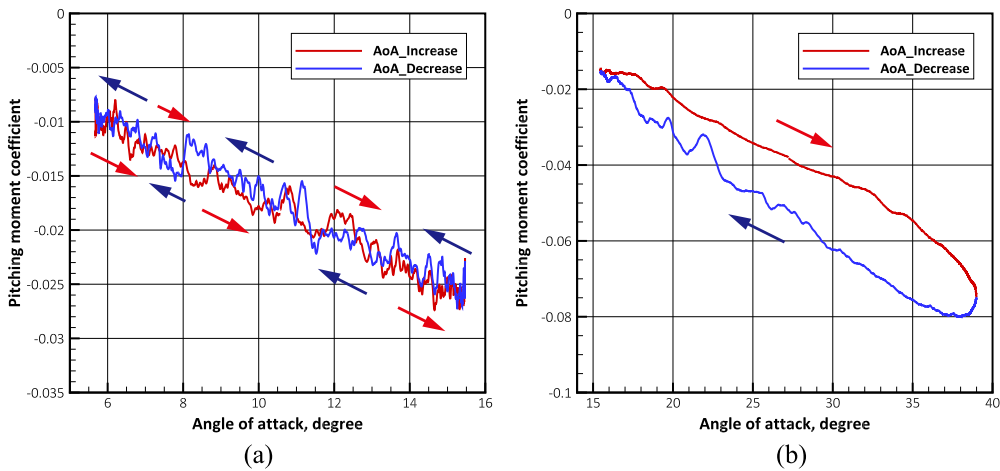


FIG. 9. Pitching moment vs AOA of SMAAC for cases of freestream Mach numbers of 0.90 and 0.13. (a) M0.90. (b) M0.13.

F. Pressure phase delay

To clarify the difference in pressure distributions between the stable and unstable cases, we obtained the pressure profiles at the front and rear surfaces and in the wake of SMAAC by using probes in the computations. Figure 10 shows the probe locations on the computed results. On the front surface, the three probes were located at the nose head and at points $\pm 0.25D$ in the z direction, where D is the diameter of SMAAC, i.e., $D = l = 1.2$ m. At the rear surface, the two probes were located at points $\pm 0.25D$ in the z direction. In the wake, we obtained the pressures at the three points where $x = 0.5D$, $1.0D$, and $1.5D$ from the nose head along the body axis in the x direction.

Figures 11(a) and 11(b) show the pressure coefficient histories at the front surface for the cases of freestream Mach numbers of 0.90 and 0.13, respectively. For M0.90, the pressures promptly followed the change in AOA, and no phase delays occurred. However, for M0.13, a noticeable phase delay in pressure at the $-0.25D$ probe point was confirmed, while none was confirmed at the nose head. This phase delay in pressure at $-0.25D$, which was caused by the pitch up motion, affected the pitching moment immediately after the AOA attained its peak. A pressure fluctuation near the highest AOA at the cycle appeared at the $+0.25D$ probe point. This was primarily attributed to the reattachment on the membrane aeroshell of the separated flow on the nose head. Therefore, the hysteresis of these pressures at the $\pm 0.25D$ probe points possibly caused instability.

Figures 12(a) and 12(b) show the pressure coefficient histories on the rear surface for the cases of freestream Mach numbers of

0.90 and 0.13, respectively. Figures 13(a) and 13(b) show the pressure coefficient histories in the wake for the cases of freestream Mach numbers of 0.90 and 0.13, respectively. The pressure histories at the rear surface were very similar to that at the $0.5D$ point in the wake. For M0.90, no remarkable structures behind the vehicle in the temporal direction were observed. We applied the FFT approach to the pressure histories. However, even the frequency of the forced oscillation did not appear, indicating that the flows at the rear and in the wake were not affected by the forced oscillation. In contrast, for M0.13, the flows behind the vehicle were clearly affected by the forced oscillation. We observed that the pressure phase was delayed with respect to change in the AOA. The pressure at $1.5D$ was particularly delayed. A similar tendency was also confirmed in Brock's study¹⁸ for the SIAD. While the phase delays at $0.5D$ and $1.0D$ points appeared at the maximum AOA, they did not appear at the minimum AOA, and pressures began to increase just before the AOA attained its minimum value. This asymmetry could become important for instability behavior.

G. Wake structure

We observed that the dynamic instability for M0.13 was caused by the phase delay in pressure. In particular, its role in the wake in response to the pitching motion was significant. Here, we visualized the second invariants of the velocity gradient tensor. Figure 14 (Multimedia view) shows a time series of an isosurface of the second invariants around SMAAC for M0.13 during a cycle between 5.000 s and 6.455 s. The figure includes the histories of pressure coefficients in the wake and AOA for M0.13 from 4.800 s to 6.800 s.

The wake behind the vehicle became small at higher AOA values and large at lower AOA values. In the wake, a recirculation region with low pressure existed a short distance from the vehicle. Vortexes formed by flows separating from the inflatable torus generated a large structure in the recirculation region. The recirculation region moved farther from the vehicle at higher AOA values

TABLE VI. Comparison of pitching moment work at each cycle and state of motion.

Case	\bar{W} (third)	\bar{W} (fourth)	\bar{W} (fifth)	State
M0.90	-0.006 761	-0.007 706	-0.012 54	Stable
M0.13	0.387 3	0.445 8	0.420 2	Unstable

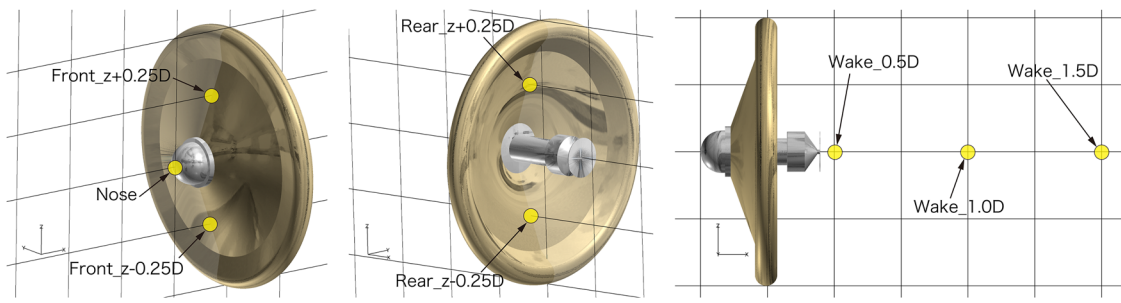


FIG. 10. Probe locations at the front and rear surfaces and in the wake.

and closer to it at lower AOA values. This region did not promptly follow the vehicle motion and a slight delay was confirmed. Flows inside the membrane aeroshell near SMAAC's rear were significantly affected by the vehicle motion. As the motion with a decrease in AOA, i.e., pitch down, began after the maximum AOA was attained [Figs. 14(c)–14(f)], air was drawn into this near-rear region from an upper region of the recirculation area and the flow in the counterclockwise direction was formed in the rear membrane aeroshell. Similarly, as the motion with an increase in AOA, i.e., pitch up, began after the minimum AOA was attained [Figs. 14(g)–14(i)], air was drawn from a lower region of the recirculation area. However, because the air inflowing from the upper region remained, impingement between upper and lower flows occurred, which induced

a pressure increase at the rear. Compared with the case at the minimum AOA, because flows at the rear promptly outflowed to the wake at the maximum AOA, a pressure increase did not occur. This difference in flows from the change in the AOA caused pressure hysteresis at the rear.

H. Instability mechanism

The pressure history demonstrated that phase delays at the front surface with the decrease in AOA and phase delays in the wake with the increase in AOA, respectively, caused dynamic instability. This did not occur for the case with a freestream Mach number of 0.90, in which the pressures promptly followed the AOA. This

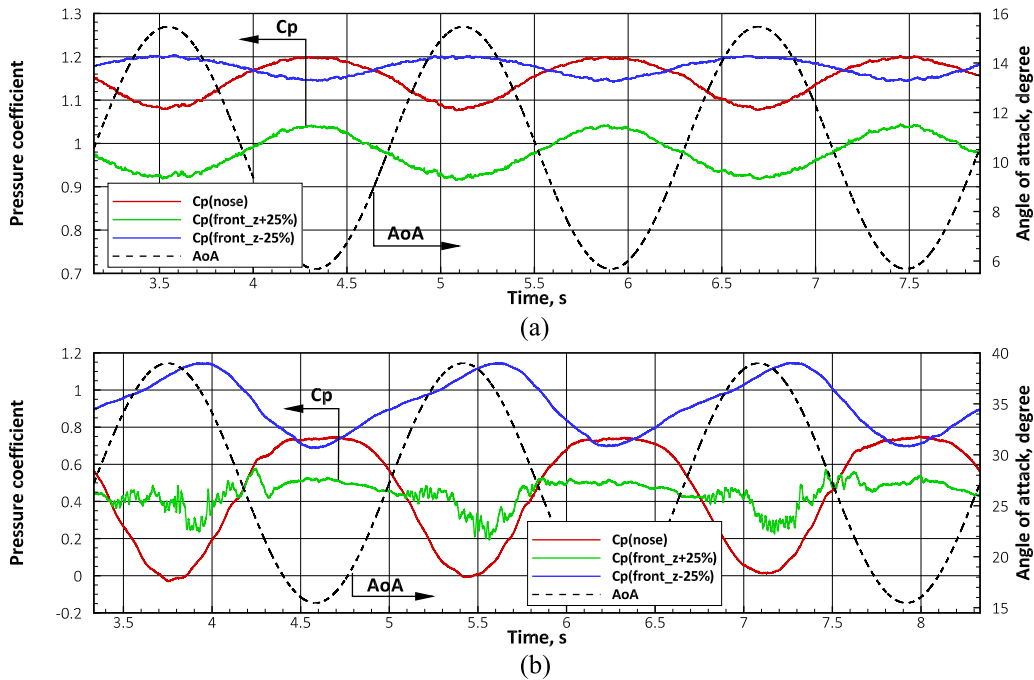


FIG. 11. Histories of pressure coefficients at the front surface of SMAAC for cases of freestream Mach numbers of 0.90 and 0.13. (a) M0.90. (b) M0.13.

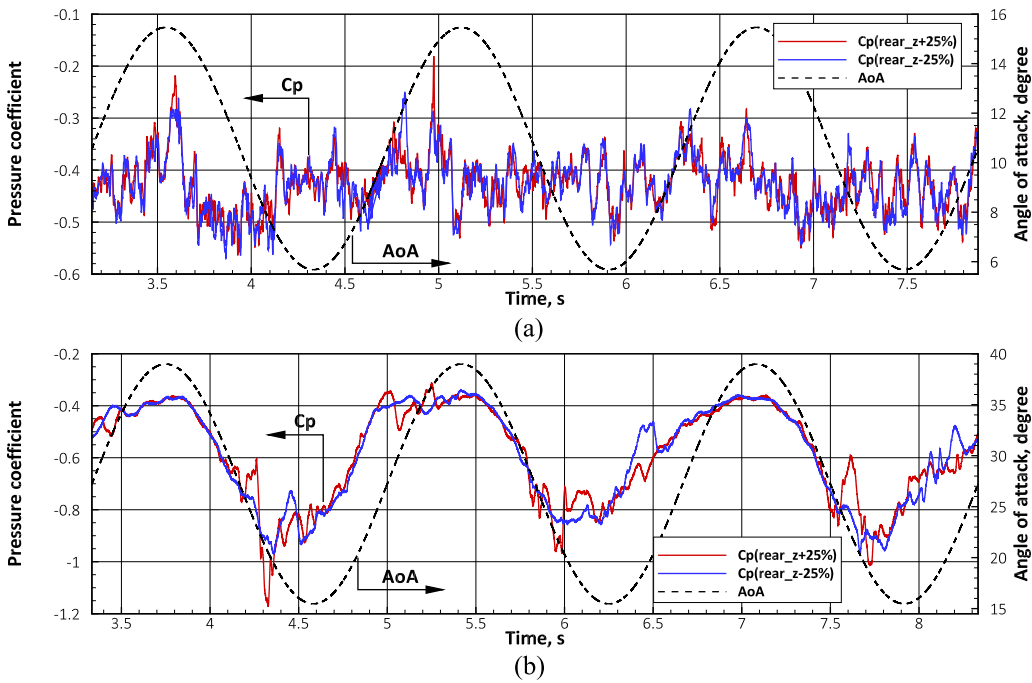


FIG. 12. Histories of pressure coefficients at the rear surface of SMAAC for scenarios of freestream Mach numbers of 0.90 and 0.13. (a) M0.90. (b) M0.13.

difference was deduced to be attributed to the reduced frequency between the two cases: $k = 0.0167$ for M0.90 and $k = 0.121$ for M0.13. For the reduced frequencies between 0.08 and 0.16 at low speed, Wang *et al.*³⁶ reported that dynamic instability occurred. The results

of this study indicated a similar structure in terms of the phase delay in the wake. Moreover, a significant aspect is that the mean angle for M0.13 became large. This caused an asymmetric structure in the wake, which resulted in instability.

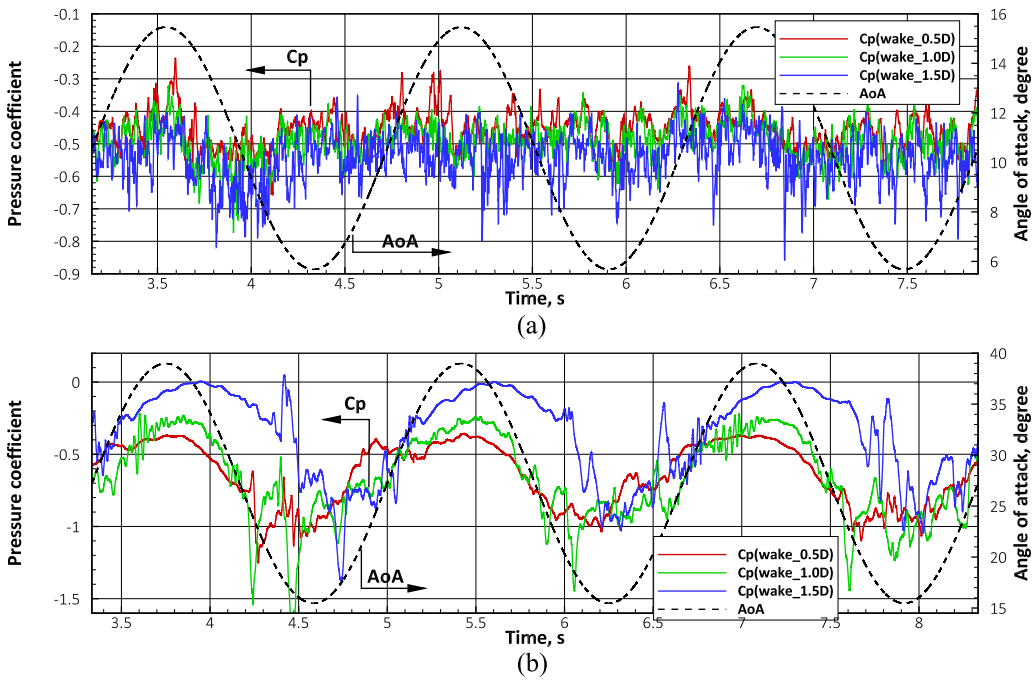


FIG. 13. Histories of pressure coefficients in the wake of SMAAC for cases of freestream Mach numbers of 0.90 and 0.13. (a) M0.90. (b) M0.13.

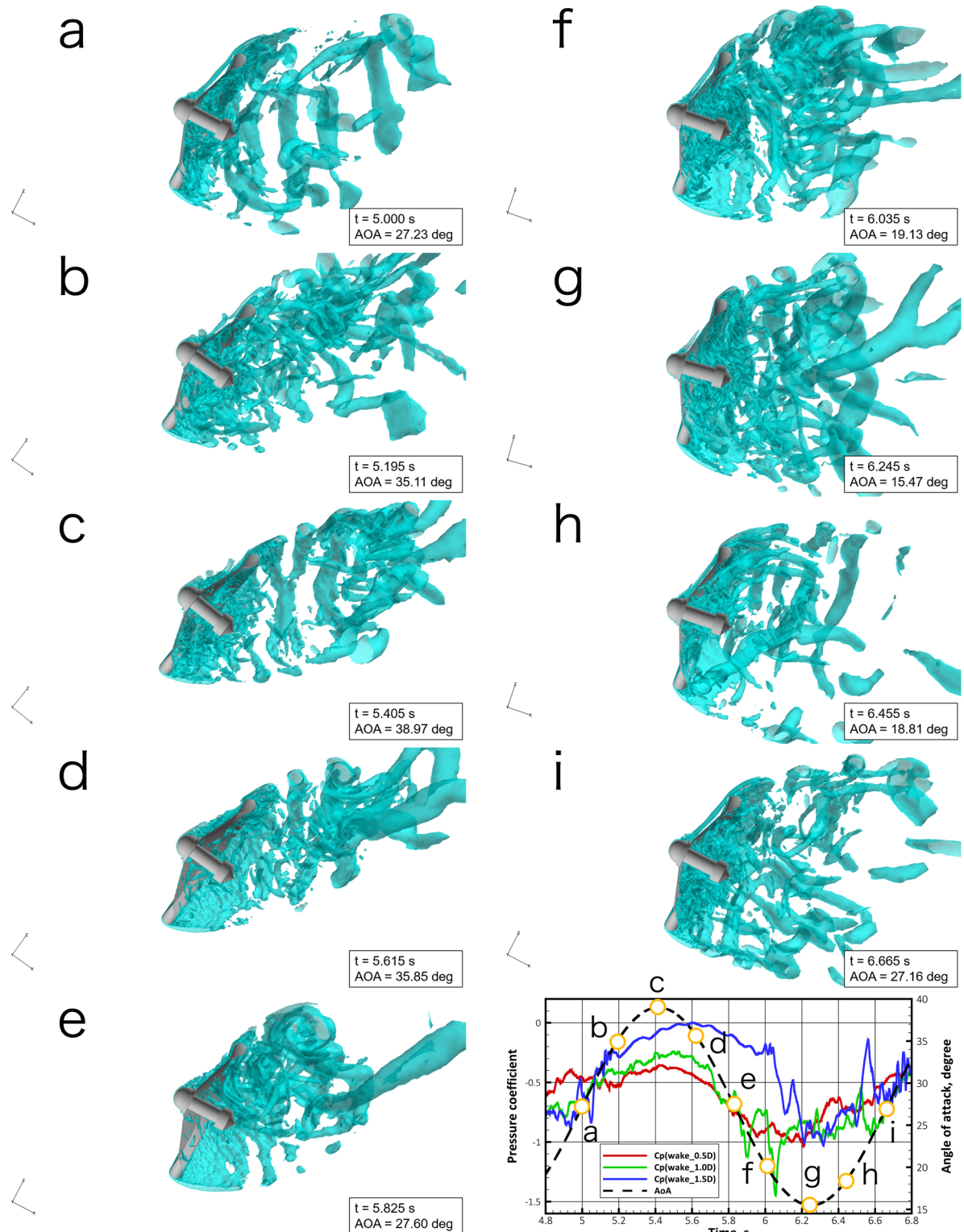


FIG. 14. Time series of second invariants of the velocity gradient tensor around SMAAC for M0.13: (a) $t = 5.000 \text{ s}$, (b) $t = 5.195 \text{ s}$, (c) $t = 5.405 \text{ s}$, (d) $t = 5.615 \text{ s}$, (e) $t = 5.825 \text{ s}$, (f) $t = 6.035 \text{ s}$, (g) $t = 6.245 \text{ s}$, (h) $t = 6.455 \text{ s}$, and (i) $t = 6.665 \text{ s}$. Multimedia view: <https://doi.org/10.1063/5.0009607.1>

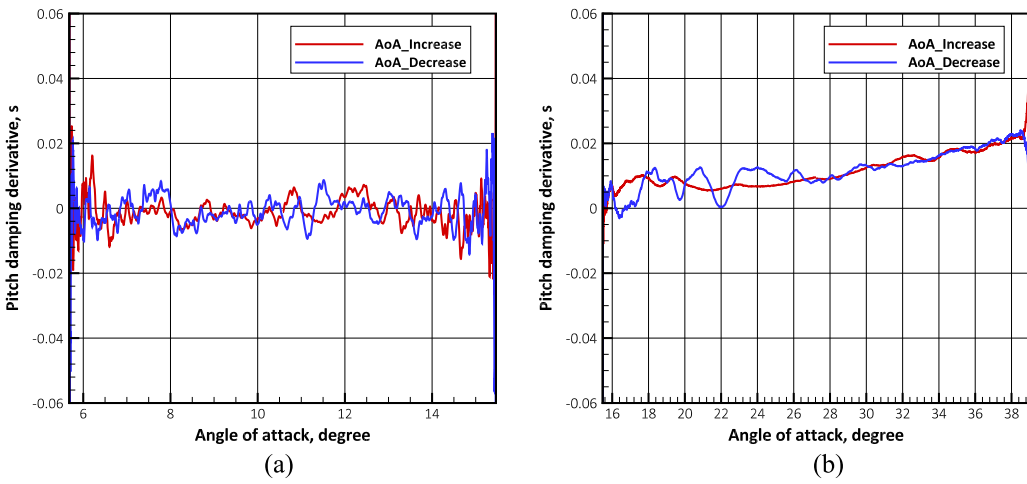


FIG. 15. Pitch damping derivatives of SMAAC for cases of freestream Mach numbers of 0.90 and 0.13. (a) M0.90. (b) M0.13.

In our simulation, only single-DOF motion was considered, whereas nutation rotation, i.e., a combination of roll and pitch motions, was also observed in the flight test. For SMAAC, the nutation rotation had minor effects in inducing severe motion such as vertical rotation. In addition, because rolling motion generally tends to increase the stability of pitching motion, motion without the roll becomes a safe assessment. For the simplicity of flow modeling in addition to the perspectives above, roll motion was not considered here; however, a multi-DOF motion will be required in future studies for a more detailed investigation.

Additionally, membrane deformation was not considered in this study. The effects on deformation were minor for aerodynamic deceleration, as reported by Takahashi *et al.*³⁷ However, deformation possibly had a significant effect on the pitching moment behavior owing to formation change. In particular, as the computed results indicated, deformation could become important for the phase delay of front pressure. In a future study, the investigation of the instability that considers membrane deformation is also required.

The CG location is an important parameter for the attitude stability of aerodynamic decelerators. In this study, no additional simulations changing the CG location for SMAAC were performed. The computed results indicated that dynamic instability for M0.13 was affected by the wake. Because this wake structure can be also affected by the location of the CG, the parameter study related to the CG may be required.

I. Damping coefficient

If the re-entry vehicle is in a single-DOF motion, the motion can be expressed by

$$I\ddot{\alpha} = \frac{1}{2}\rho_\infty U_\infty^2 S I \{ C_{M\alpha}(\alpha - \alpha_0) + (C_{Mq} + C_{M\dot{\alpha}})\dot{\alpha} \}, \quad (19)$$

where $C_{M\alpha}$ and $(C_{Mq} + C_{M\dot{\alpha}})$ are the pitch static and pitch damping derivatives, respectively. Evaluating the pitch damping derivative of the motion is important for designing and developing re-entry

vehicles. We expanded the pitching moment coefficient of motion in a single DOF around the angular velocity of $\dot{\alpha} = 0$. If terms higher than second order are assumed to be negligible, we can express the pitching moment coefficient by

$$C_M = C_{M0} + C_{M\alpha}\alpha + (C_{Mq} + C_{M\dot{\alpha}})\dot{\alpha}. \quad (20)$$

The first and second terms on the right-hand side of the above equation correspond to the pitching moment coefficient in the static state. Here, these were obtained by the linear approximation of the pitching moment coefficient in each cycle.

Figures 15(a) and 15(b) show the pitch damping derivatives of SMAAC for the cases of freestream Mach numbers of 0.90 and 0.13, respectively. These derivatives were averaged over the three cycles between the third and fifth cycles. For M0.90, the damping derivative tended to be slightly negative although oscillation was observed. This meant that damping occurred for the system of motion, which was confirmed in the flight test. However, for M0.13, the damping derivative tended to be positive. In particular, it became large at higher AOA values, which meant that the instability of the motion was enhanced at higher AOA values.

IV. CONCLUSIONS

We numerically investigated the aerodynamic instability of an inflatable re-entry vehicle, which was observed at low-Mach-number speeds in a suborbital re-entry mission. To reproduce the pitch oscillation motion of the vehicle in the unsteady turbulent flow field, we adopted a large-eddy simulation approach with forced oscillations. Computed results were obtained for two representative cases of freestream Mach numbers of 0.90 (M0.90) and 0.13 (M0.13), which were in stable and unstable states during the flight, respectively.

The computed pitching moment histories indicated that the vehicle was stable in attitude for M0.90 but unstable for M0.13. Because the vehicle attitude was statically stable at all speeds, this behavior was caused by dynamic instability. The work produced by

the pitching moment acting on the AOA of the vehicle was positive for M0.13, indicating a dynamically unstable state. From pressure histories at the front and rear surfaces and in the wake of the vehicle, phase delays of pressure were confirmed for M0.13, whereas no delay occurred for M0.90. In particular, for M0.13, the front surface pressure significantly affected the phase delay as the AOA decreased, while the pressure in the wake had a significant effect on the phase delay as the AOA increased. We observed that vortexes behind the vehicle that were formed by flows separating from the inflatable torus moved with a delay following the vehicle motion. Dynamic instability resulted from flow behaviors that could not promptly follow the vehicle motion.

ACKNOWLEDGMENTS

This work was supported by the JSPS KAKENHI (Grant No. 17KK0123). The presented computational results were obtained using the fast unstructured CFD code “FaSTAR,” which was developed by JAXA. This work was supported by the “Advanced Computational Scientific Program” of the Research Institute for Information Technology, Kyushu University.

DATA AVAILABILITY

The data that support the findings of this study are available from the corresponding author upon reasonable request.

REFERENCES

- ¹T. Abe, “A self-consistent tension shell structure for application to aerobraking vehicle and its aerodynamic characteristics,” AIAA Paper No. 1988-3405, 1988.
- ²Y. Takahashi and K. Yamada, “Aerodynamic heating of inflatable aeroshell in orbital reentry,” *Acta Astronaut.* **152**, 437–448 (2018).
- ³Y. Takahashi, K. Yamada, and T. Abe, “Examination of radio frequency blackout for an inflatable vehicle during atmospheric reentry,” *J. Spacecr. Rockets* **51**(2), 430–441 (2014).
- ⁴I. G. Clark, A. L. Hutchings, C. L. Tanner, and R. D. Braun, “Supersonic inflatable aerodynamic decelerators for use on future robotic missions to mars,” *J. Spacecr. Rockets* **46**(2), 340–352 (2009).
- ⁵S. J. Hughes, D. F. M. Cheatwood, A. M. Calomino, and H. S. Wright, “Hypersonic inflatable aerodynamic decelerator (HIAD) technology development overview,” AIAA Paper No. 2011-2524, 2011.
- ⁶M. Gräßlin and U. Schöttle, “Flight performance evaluation of the reentry mission IRDT-1,” in Papers presented at the 52nd International Astronautical Congress, IAF Paper 01-V305, Toulouse, France, 1–5 October 2001.
- ⁷K. Yamada, Y. Nagata, T. Abe, K. Suzuki, O. Imamura, and D. Akita, “Suborbital reentry demonstration of inflatable flare-type thin-membrane aeroshell using a sounding rocket,” *J. Spacecr. Rockets* **52**(1), 275–284 (2015).
- ⁸Y. Nagata, K. Yamada, T. Abe, and K. Suzuki, “Attitude dynamics for flare-type membrane aeroshell capsule in reentry flight experiment,” AIAA Paper No. 2013-1285, 2013.
- ⁹Y. Takahashi, K. Yamada, T. Abe, and K. Suzuki, “Aerodynamic heating around flare-type membrane inflatable vehicle in suborbital reentry demonstration flight,” *J. Spacecr. Rockets* **52**(6), 1530–1541 (2015).
- ¹⁰T. Ohashi, Y. Takahashi, H. Terashima, and N. Oshima, “Aerodynamic instability of flare-type membrane inflatable vehicle in suborbital reentry demonstration,” *J. Fluid Sci. Technol.* **13**(3), JFST0020 (2018).
- ¹¹C. D. Kazemba, R. D. Braun, I. G. Clark, and M. Schoenberger, “Survey of blunt-body supersonic dynamic stability,” *J. Spacecr. Rockets* **54**(1), 109–127 (2017).
- ¹²K. Hiraki, Transonic dynamic instability of disk-shaped capsule, The Institute of Space and Astronautical Science report. SP Aerodynamics, Thermophysics, Thermal Protection, Flight System Analysis and Design of Asteroid Sample Return Capsule, 2003, Vol. 17, p. 265.
- ¹³S. Teramoto, K. Hiraki, and K. Fujii, “Numerical analysis of dynamic stability of a reentry capsule at transonic speeds,” *AIAA J.* **39**(4), 646–653 (2001).
- ¹⁴S. Teramoto and K. Fujii, “Mechanism of dynamic instability of a reentry capsule at transonic speeds,” *AIAA J.* **40**(12), 2467–2475 (2002).
- ¹⁵T. Tsurumoto, Y. Takahashi, H. Terashima, and N. Oshima, “Numerical analysis of aerodynamic instability for HAYABUSA type reentry capsule,” in 8th European Conference for Aeronautics and Space Sciences (EUCASS), 2019.
- ¹⁶S. Koga, A. Hidaka, R. Tagai, T. Kimura, T. Yoshihaga, S. Nagai, and H. Nishijima, “Dynamic stability testing of a reentry lifting capsule in a transonic wind tunnel,” in *52nd Aerospace Sciences Meeting* (AIAA, 2014), p. 1119.
- ¹⁷A. Hashimoto, K. Murakami, T. Aoyama, R. Tagai, S. Koga, S. Nagai, and K. Hayashi, “Dynamic stability analysis of a reentry lifting capsule with detached eddy simulation,” in *54th AIAA Aerospace Sciences Meeting* (AIAA, 2016), p. 0552.
- ¹⁸J. M. Brock, E. Stern, and M. C. Wilder, “Dynamic CFD simulations of the supersonic inflatable aerodynamic decelerator (SAID) ballistic range tests,” in *55th AIAA Aerospace Sciences Meeting* (AIAA, 2017), p. 1437.
- ¹⁹Y. Ohmichi, T. Ishida, and A. Hashimoto, “Modal decomposition analysis of three-dimensional transonic buffet phenomenon on a swept wing,” *AIAA J.* **56**(10), 3938–3950 (2018).
- ²⁰J. Kou and W. Zhang, “Dynamic mode decomposition with exogenous input for data-driven modeling of unsteady flows,” *Phys. Fluids* **31**(5), 057106 (2019).
- ²¹Y. Ohmichi, K. Kobayashi, and M. Kanazaki, “Numerical investigation of wake structures of an atmospheric entry capsule by modal analysis,” *Phys. Fluids* **31**(7), 074105 (2019).
- ²²R. M. J. Kramer, F. Cirak, and C. Pantano, “Fluid-structure interaction simulations of a tension-cone inflatable aerodynamic decelerator,” *AIAA J.* **51**(7), 1640–1656 (2013).
- ²³J. Guo, G. Lin, X. Bu, S. Fu, and Y. Chao, “Effect of static shape deformation on aerodynamics and aerothermodynamics of hypersonic inflatable aerodynamic decelerator,” *Acta Astronaut.* **136**, 421–433 (2017).
- ²⁴A. Favre, “Turbulence: Space-time statistical properties and behavior in supersonic flows,” *Phys. Fluids* **26**(10), 2851–2863 (1983).
- ²⁵E. Garnier, N. Adams, and P. Sagaut, *Large Eddy Simulation for Compressible Flows* (Springer Science & Business Media, 2009).
- ²⁶J. Smagorinsky, “General circulation experiments with the primitive equations,” *Mon. Weather Rev.* **91**(3), 99–164 (1963).
- ²⁷M. L. Shur, P. R. Spalart, M. K. Strelets, and A. K. Travin, “A hybrid RANS-LES approach with delayed-DES and wall-modelled LES capabilities,” *Int. J. Heat Fluid Flow* **29**(6), 1638–1649 (2008).
- ²⁸Y. Takahashi, “Advanced validation of CFD-FDTD combined method using highly applicable solver for reentry blackout prediction,” *J. Phys. D: Appl. Phys.* **49**(1), 015201 (2016).
- ²⁹A. Hashimoto, K. Murakami, T. Aoyama, K. Ishiko, M. Hishida, M. Sakashita, and P. R. Lahur, “Toward the fastest unstructured CFD code ‘FaSTAR’,” AIAA Paper No. 2012-1075, 2012.
- ³⁰E. Shima and K. Kitamura, “Parameter-free simple low-dissipation AUSM-family scheme for all speeds,” *AIAA J.* **49**(8), 1693–1709 (2011).
- ³¹J. Chen, A. Ghosh, K. Sreenivas, and D. Whitfield, “Comparison of computations using Navier-Stokes equations in rotating and fixed coordinates for flow through turbomachinery,” in *35th Aerospace Sciences Meeting and Exhibit* (AIAA, 1997), p. 878.
- ³²P. D. Thomas and C. K. Lombard, “Geometric conservation law and its application to flow computations on moving grids,” *AIAA J.* **17**(10), 1030–1037 (1979).
- ³³R. E. Gordnier and M. R. Visbal, “Development of a three-dimensional viscous aeroelastic solver for nonlinear panel flutter,” *J. Fluids Struct.* **16**(4), 497–527 (2002).

³⁴F. Nicoud and F. Ducros, “Subgrid-scale stress modelling based on the square of the velocity gradient tensor,” *Flow, Turbul. Combust.* **62**(3), 183–200 (1999).

³⁵J. Monteiro, S. Paris, L. Peveroni, and P. Rambaud, “On the validation of experimental results for the dynamic stability of re-entry capsules,” *Aerosp. Sci. Technol.* **52**, 224–233 (2016).

³⁶F. Y. Wang, O. Karatekin, and J.-M. Charbonnier, “Low-speed aerodynamics of a planetary entry capsule,” *J. Spacecr. Rockets* **36**(5), 659–667 (1999).

³⁷Y. Takahashi, D. Ha, N. Oshima, K. Yamada, T. Abe, and K. Suzuki, “Aerodecelerator performance of flare-type membrane inflatable vehicle in suborbital reentry,” *J. Spacecr. Rockets* **54**(5), 993–1004 (2017).